



# Co<sub>3</sub>O<sub>4</sub> negative electrode material for rechargeable sodium ion batteries: An investigation of conversion reaction mechanism and morphology-performances correlations



Gianluca Longoni<sup>a</sup>, Michele Fiore<sup>a</sup>, Joo-Hyung Kim<sup>b</sup>, Young Hwa Jung<sup>b</sup>, Do Kyung Kim<sup>b</sup>, Claudio M. Mari<sup>a</sup>, Riccardo Ruffo<sup>a,\*</sup>

<sup>a</sup> Dipartimento di Scienza dei Materiali, Università degli Studi di Milano Bicocca, via Cozzi 55, Milano, Italy

<sup>b</sup> Department of Materials Science and Engineering, Korea Advanced Institute of Science and Technology (KAIST), 291 Daehak-ro, Yuseong-gu, Daejeon, Republic of Korea

## HIGHLIGHTS

- The reversible electrochemical reaction mechanism involves CoO instead of Co<sub>3</sub>O<sub>4</sub>.
- Electrode presodiation decreases noticeably the first cycle capacity loss.
- Presodiated electrode shows a capacity of 600 mAh g<sup>-1</sup> after 50 cycles.

## ARTICLE INFO

### Article history:

Received 30 June 2016

Received in revised form

7 September 2016

Accepted 16 September 2016

### Keywords:

Cobalt oxide

Sodium ion batteries

Electrode materials

## ABSTRACT

Transition metal oxides have recently aroused a renewed and increasing interest as conversion anode materials for sodium ion batteries. Being their electrochemical performances strongly dependent on morphological aspects, has been here proposed a straightforward approach to modulate morphological characteristics of a transition metal oxide (Co<sub>3</sub>O<sub>4</sub>) using a low cost synthetic route. The as obtained optimized morphology allows the realization of high practical specific capacities, higher than 500 mAh g<sup>-1</sup> after 50 cycles, and represents a valid candidate for further optimization. In addition to the morphology-performance correlations, the reaction mechanism beyond the electrochemical behavior was also investigated revealing the role of the CoO phase in the charge/discharge process. Finally, an electrode pre-sodiation treatment for conversion materials is presented: it has been indeed demonstrated that it sensibly decreases the irreversible capacity correlated to the first cycle and improves cycle ability.

© 2016 Elsevier B.V. All rights reserved.

## 1. Introduction

Lithium-ion battery (LIB) technology has ended to cover, in almost 25 years, the 95% of the secondary battery market for cordless device (mobile phones, laptops, cameras, working tools) [1] thanks to its versatility, high round trip efficiency and adequate energy density. Its market permeability also relates to automotive field, where a high energy density is desirable over a high power density. The recent introduction of LIBs to cars propulsion (Hybrid

electric vehicles HEV, Plug-in hybrid electric vehicle PHEV, and Electric vehicles EV) is expected to lead in a few years to a dramatic increase in LIBs technology exploitation. This aspect, together with political issues related to in-homogeneity distribution of raw materials for LIB manufacturing, concurred to arise a growing concern in relation to the future sustainability of this technology [2–4]. The sodium-ion battery (SIB) system seems to be a valid and more sustainable alternative to Lithium economy, according to the easier procurement of raw materials and the rather similar chemistry between Li and Na [5,6]. SIBs would be a better choice, especially for large scale application, such as stationary storage connected to renewable power sources, in which costs are critical [7]. Developing efficient SIBs worthwhile to be employed in on-grid storage and other fields may lower the exploitation load over LIBs technology,

\* Corresponding author. Dipartimento di Scienza dei Materiali, Università degli Studi di Milano Bicocca, via Cozzi 55, 20125, Milano, Italy.

E-mail address: [riccardo.ruffo@unimib.it](mailto:riccardo.ruffo@unimib.it) (R. Ruffo).

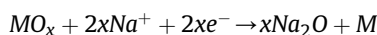
reducing the strategic interest for the raw materials.

Many efforts have already been made in the design and characterization of both anode and cathode materials for Na-ion batteries so far [8,9]. For what concern cathode side of SIBs, promising results have been achieved in relation to the stability and charge retention of electroactive intercalation materials as widely described in the review by Masquelier et al. [10].

In this extensive dissertation the authors go through several promising polyanionic ( $(\text{PO}_4)^{2-}$ ,  $(\text{SiO}_4)^{4-}$  and  $(\text{SO}_4)^{2-}$ ) based compounds proposed in recent years as cathode materials in LIBs, in the place of fully investigated transition metal oxides ( $\text{Li}_{1-x}\text{MO}_2$  with  $M = \text{Co, Ni, Fe, Mn}$ ). The performances of the latter in a Na environment are also collected. As a result, polyanion frameworks are capable of an efficiently sodium cations intercalation, with a high structure retention through cycling. The advantages in their utilization resides also in the polyanion inductive effect that boosts the cathode operating voltage, higher stability, large variety of obtainable structure and atoms arrangements and the lower costs of manufacturing. Anode materials, conversely, still represent a challenging topic needly to be investigated. Many solutions have been proposed to overcome the intrinsic limits of negative electrode materials, namely the low practical specific charge and the fast degradation of electrode characteristics. Other delicate features that have to be taken into consideration are the operating voltage, that must be suitable for the utilization of the investigated compound as an anode inside the cell and the problematic irreversible capacity related to the first cycle. For these reasons several classes of materials have been taken into account [6,11]. Transposition of graphitic anodes already employed in LIBs to sodium environment has been considered at first glance: nevertheless, since intercalation of the larger sodium ion into graphite sheets structure induces exfoliation, nano-structured hard-carbons have been investigated instead [12–14]. The performances are controversial and are affected by high irreversible capacity during the first charge/discharge loop and sloping charge/discharge profiles. Sodium alloying with 14th and 15th group elements (Sb [15,16], Sn [17], Ge and In [18]) has been also exploited to obtain anode materials for SIBs: the high theoretical capacity of sodium rich phase Na-Sn alloy ( $847 \text{ mAh g}^{-1}$  for  $\text{Na}_{15}\text{Sn}_4$ ) led to the study of the performances in sodium half-cell of a SnSb particles dispersion over a carbonaceous matrix. Xiao et al. obtained a reversible alloying of Na and a stable capacity of  $\sim 400 \text{ mAh g}^{-1}$  [19].

Transition metal oxides ( $\text{MO}_x$  with  $M = \text{Fe}$  [20],  $\text{Co}$  [21],  $\text{Cu}$  [22]), with electrochemical active transition metal ions, have drawn the attention as possible low cost and easy-to-manufacture SIB conversion anode materials. Their reactivity, electrochemical performances, and effects of morphology and structural properties on lithium storage, have been widely analyzed. On the contrary, same type of studies related to reactivity with Na, remain poorly explored. The study of Na reactivity with spinel  $\text{Co}_3\text{O}_4$  nanoparticles has been recently reported by few groups, and a first understanding of the possible undergoing conversion mechanism has been hypothesized.

The general reaction proposed for the sodium reactivity with spinel type oxides and other conversion materials is the following [11]:



Notable aspects of the reaction above reported are its reversibility and the theoretical capacity of oxides ( $>600 \text{ mAh g}^{-1}$ ), considerably higher if compared to carbonaceous materials or intercalation materials for which capacity is limited by the number of available sites for  $\text{Na}^+$  insertion [6] ( $\sim 300 \text{ mAh g}^{-1}$ ). Spinel  $\text{Co}_3\text{O}_4$ , thanks to its high theoretical capacity ( $\sim 890 \text{ mAh g}^{-1}$ ), has aroused,

since the early stages of LIB technology development, a great interest as a high capacity conversion anode material [21,23,24]. Along with the advantage of having a high theoretical capacity comes also the challenge represented by the large particle volume variation during sodiation which leads rapidly to a considerable fade in material properties. In a recent work by Sun et al. a  $\text{Co}_3\text{O}_4$  porous particles/graphene compound has been investigated as active anode material in a sodium ion battery [25]. The hybrid compound ensured a good capacity ( $\sim 500 \text{ mAh g}^{-1}$ ) and good cycle stability at the current density of  $25 \text{ mA g}^{-1}$ . Owing to the volume variation connected to conversion mechanism, morphology of active material particles acquires a primary importance. Crystal shape, exposed facets, hierarchical structures and porosity of particles are essential features to be taken into consideration when it comes to minimize the deleterious effect of excessive volume change induced stresses. Effect of different morphology of  $\text{Co}_3\text{O}_4$  particles over the electrochemical performances has been highlighted in the case of lithium batteries, and the better performances of polycrystalline hierarchical structure compared to single nanocrystals has been confirmed [26]. Another negative aspect related to conversion materials is the irreversible capacity involved in the first charge/discharge loop. It determines a significant drop in the residual capacity available for the following cycles. By many, this behavior has been addressed to the SEI formation which involves a non-negligible amount of active species.

In the present work, three different morphologies of spinel  $\text{Co}_3\text{O}_4$  have been prepared. These have been synthesized using facile and easily scalable synthetic routes and they have been deeply investigated under the electrochemical point of view as anode materials in metallic sodium half-cells; conclusions related to the morphology influence have thus been made. Moreover, the characteristic conversion mechanism beyond the electrochemical reaction with sodium has been studied. Finally, the problem related to the first cycle irreversible capacity has also been tackled. In particular, the effect of a chemical pre-sodiation of the  $\text{Co}_3\text{O}_4$  electrode has been taken into consideration.

## 2. Experimental

### 2.1. Synthesis

Hydrothermal synthesis technique is known to be a versatile synthetic route that allows to obtain a large variety of different morphologies by changing operating conditions, namely temperature, volume (fill factor), hydrothermal step time, precursor and capping agents concentration and pH [24,26]. In studying spinel  $\text{Co}_3\text{O}_4$  morphology effects over the electrochemical behavior, several structures have been prepared and tested. In this work, the preparation and characterization of just the three most significant ones, according to their electrochemical performances, are reported. The three samples are here listed with their codes:  $\text{CO}_S$  (cobalt oxide slabs),  $\text{CO}_N$  (cobalt oxide needles),  $\text{CO}_F$  (cobalt oxide flakes). All the chemicals were of analytical grade and were used as received. The cobalt precursor,  $\text{Co}(\text{NO}_3)_2 \cdot 6\text{H}_2\text{O}$  (ACS reagent,  $\geq 98\%$ , Sigma-Aldrich<sup>®</sup>) has been dissolved in deionized water together with  $\text{CO}(\text{NH}_2)_2$  (ACS reagent, Sigma-Aldrich<sup>®</sup>), used as a mineralizing agent, and the solution has been transferred to a 100 mL Teflon-lined stainless steel autoclave. The autoclave has been heated starting from room temperature using a heating rate of  $4^\circ \text{ min}^{-1}$ , and after dwelling at the set-point temperature (according to the synthetic route) it has been let to cool down naturally to room temperature again. The operational parameters for the three samples mentioned above are reported in Table 1. After the hydrothermal step the intermediate was collected by centrifugation from the autoclave, washed several times with deionized

water and ethanol and dried in an oven at 60 °C, overnight. The obtained product underwent calcination in air at 400 °C for 12 h.

## 2.2. Samples characterization

Samples morphology was evaluated using a SEM (HITACHI, S-4800) and TEM (FEI, Tecnai G<sup>2</sup> F30 S-Twin) micrographs, while the crystal phases of the samples were checked via X-ray powder diffraction using a Rigaku diffractometer (D/Max-2500, 0.154 nm Cu K- $\alpha$  radiation). The diffraction patterns were collected in the 2 $\theta$  window between 15° and 70°, at 3° min<sup>-1</sup> scan rate. In order to monitor the active material phase changes over cycles, X-ray diffraction has been performed on cycled electrodes. XRD measurements on electrodes have been performed using a Rigaku MiniFlex 600 diffractometer (0.154 nm Cu K- $\alpha$  radiation). For this analysis the diffraction patterns were collected in the 2 $\theta$  window between 20° and 80°, at 3° min<sup>-1</sup> scan rate. AAS (Atomic Absorption Spectroscopy) elemental analysis (microCUBE, Elementar) was employed to estimate the amount of sodium included in the pre-sodiated sample in relation to the electrode exposure time to metallic sodium.

## 2.3. Electrochemical measurements

Electrodes for electrochemical measurements were assembled by mixing the as prepared active material (nanostructured Co<sub>3</sub>O<sub>4</sub>) with a carbon matrix (Super P MIM Carbon) and polyacrylic acid (average M<sub>v</sub> ~450000, Sigma-Aldrich®) as binder, with the weight ratio of 75:17:8. As dispersing solvent, 1-methyl-2-pyrrolidinone (ACS reagent, 99%, Aldrich®) was employed. Polyacrylic acid has been chosen as the binder according to the recent findings concerning the binder-active material coupling [27]. Polyacrylic acid better accommodates volume change-related mechanical stresses of oxide-based materials than PVDF, a well-known binder employed in lithium-ion batteries electrode formulation were the active material is typically an intercalation material. The obtained slurry was film casted onto a copper foil and the deposition was then let to dry to the complete evaporation of the solvent, in a vacuum oven at 80 °C. The film was thus roll-pressed and 10 mm diameter disks were punched out to be used as positive electrodes in half-cells. Load of active material on each electrode was always included between 0.5 and 1 mg cm<sup>-2</sup>. All the electrochemical tests were performed in a three electrodes Swagelok type half-cells, assembled in an argon-filled glove box (Mbraun). The electrolyte employed was a propylene carbonate ( $\geq$ 99.9%, Merck) 1 M NaClO<sub>4</sub> (ACS reagent,  $\geq$ 98%, Sigma-Aldrich®) solution with 2% wt fluoroethylene carbonate (99%, Aldrich®) addition. The electrolyte solution was immobilized onto a glass fiber disk used as the separator. Sodium metal (99.9%, trace metal basis, Sigma-Aldrich®) disks were employed as counter electrode as well as reference electrode.

## 2.4. Electrode sodiation

For what concern the chemical pre-sodiation of the electrodes, a metallic sodium disk (99.9%, trace metal basis, Sigma-Aldrich®) was placed in direct contact with the cobalt oxide containing electrode,

previously wetted with the electrolyte, and held in place for an interval of time. After this step, the electrode was assembled in the electrochemical cell as already described, and subjected to electrochemical characterization.

## 3. Results and discussion

In Fig. 1, XRD patterns of the as-prepared samples are reported. Phase purity is confirmed and diffraction peaks have been addressed to the cubic phase of Co<sub>3</sub>O<sub>4</sub> spinel, identified by the space group *Fd-3m* (ICDD card No. 00-043-1003).

The morphological comparison among the three proposed samples is presented in Fig. 2, where SEM and TEM micrographs are displayed. Differences in the morphology are substantial and are mainly related to the way the primary nanometric sized crystallites, whose presence is appreciable in TEM images (image d, e and f in Fig. 2), assemble in secondary structures. In the case of CO<sub>S</sub>, large slabs (several square micrometers wide and hundreds of nanometers thick) were obtained. Further magnification of slab edges reveals the highly porous nature of the secondary structure. Among the platelets, nanometric octahedral crystals can be also spotted. Needles like secondary structures were obtained in the case of CO<sub>N</sub>, as can be noted in image b and e in Fig. 2. Each needle is hundreds of nanometers long and between 20 and 50 nanometers wide, and is composed by coagulated globular crystallites forming rows. CO<sub>F</sub> particles (image c and f), eventually, assumed a flake-like morphology, characterized by high porosity. Pores diameter can be assessed from TEM micrographs in the case of CO<sub>S</sub> and CO<sub>F</sub>, while CO<sub>N</sub> doesn't always show an appreciable 3D porosity owing the poor 3D domain of needle-like structure. In both cases (CO<sub>S</sub> and CO<sub>F</sub>) pores dimensionality falls in the mesopore regime, with the pores width never exceeding 50 nm (Fig. 3). In CO<sub>S</sub> case, pores appear to be slightly smaller compared to CO<sub>F</sub> pores. Pore dimensions have been evaluated statistically by taking measurement directly on TEM images, as illustrated in Fig. 3. The difference in pore dimensionality can be ascribed to urea utilization during synthesis. It can be noted how the use of urea as the mineralizing agent drives the formation of smaller pores (CO<sub>S</sub> and CO<sub>N</sub>). This positive aspect can be related to the slow hydrolysis urea undergoes in a hydrothermal environment compared to other Bronsted bases, such as NaOH [28]. The slow hydrolysis leads to low grades of super saturation during precipitation of cobalt compounds primary particles, and this translates in a better packing of them forming a secondary structure with finer porosity. Temperature, instead, has clearly a direct effect onto the formation of complex structure extended in the 3D domain. The cooling down of the autoclave, performed always at the same rate, drives the growth of secondary structure accordingly to the starting temperature: the higher the temperature, the more extended the secondary structure. This well explains the low dimensionality of CO<sub>N</sub>, synthesized at low temperature, 100 °C. The mesopores domain has been described as being a favourable feature in conversion materials for sodium storage, according to the facilitation in mass diffusion/transport and exposing a high active surface area [25]. For all the samples, primary round-shaped particles appear to be highly crystalline, as suggested by the TEM diffraction patterns (insets in Fig. 3).

**Table 1**  
Hydrothermal step synthetic parameters.

Sample	Co(NO <sub>3</sub> ) <sub>2</sub> ·6H <sub>2</sub> O mol L <sup>-1</sup>	CO(NH <sub>2</sub> ) <sub>2</sub> mol L <sup>-1</sup>	Autoclave fill factor/%	Hydrothermal step
CO <sub>S</sub>	0.023	0.12	70	160 °C, 12 h
CO <sub>N</sub>	0.022	0.11	85	100 °C, 12 h
CO <sub>F</sub>	0.12	–	85	180 °C, 5 h

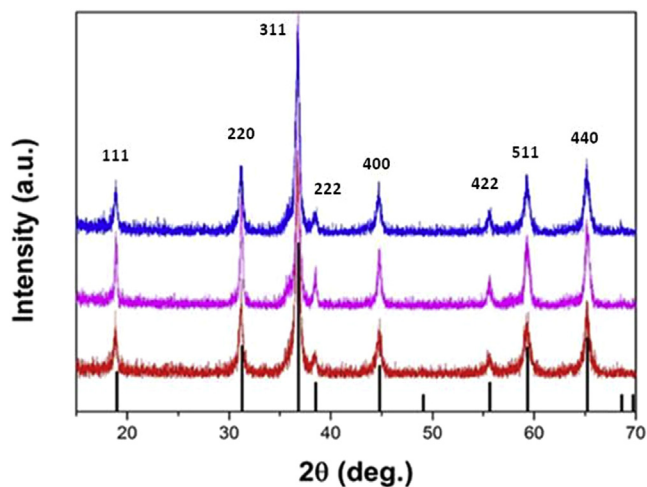


**Fig. 1.** XRPD patterns of the as prepared  $\text{Co}_3\text{O}_4$  samples:  $\text{CO}_5$  (red),  $\text{CO}_N$  (purple) and  $\text{CO}_F$  (blue). (For interpretation of the references to colour in this figure legend, the reader is referred to the web version of this article.)

For this reason round shaped primary particle, which do not show a net prevalence of a crystal facet over the others, are obtained and no octahedral crystallites were spotted in the  $\text{CO}_5$  sample.

Primary direct consequences of morphology discrepancies can be observed in galvanostatic cycling trends (Fig. 4a). Tests have been taken at the C-rate of 0.1 C ( $89 \text{ mA g}^{-1}$ ), at  $25^\circ\text{C}$ . It can be noted that while  $\text{CO}_5$  and  $\text{CO}_F$  show a gradual and constant decrease in specific capacity,  $\text{CO}_N$  shows a higher capacity and a milder decrease in capacity retention over cycles. After 50 cycles,  $\text{CO}_N$  can still provide  $360 \text{ mAh g}^{-1}$  against 220 and  $167 \text{ mAh g}^{-1}$  for  $\text{CO}_5$  and  $\text{CO}_F$  respectively. In order to highlight the occurring processes, charge/discharge profiles for  $\text{CO}_N$  has been reported in Fig. 4b. The curves are reported in the potential window ranging from 0.01 to 3.00 V vs.  $\text{Na}/\text{Na}^+$ , and the capacities are normalized over the mass of the active material alone, namely  $\text{Co}_3\text{O}_4$  (with  $890 \text{ mAh g}^{-1}$  theoretic specific capacity). According to many works reported in literature, a high irreversible capacity is registered during the first sodiation/de-sodiation (black curve Fig. 4b) [25,30,31]. Quantitatively, close to the 30% of initial sodiation capacity is not recovered during the following desodiation step. For what concern the ca-

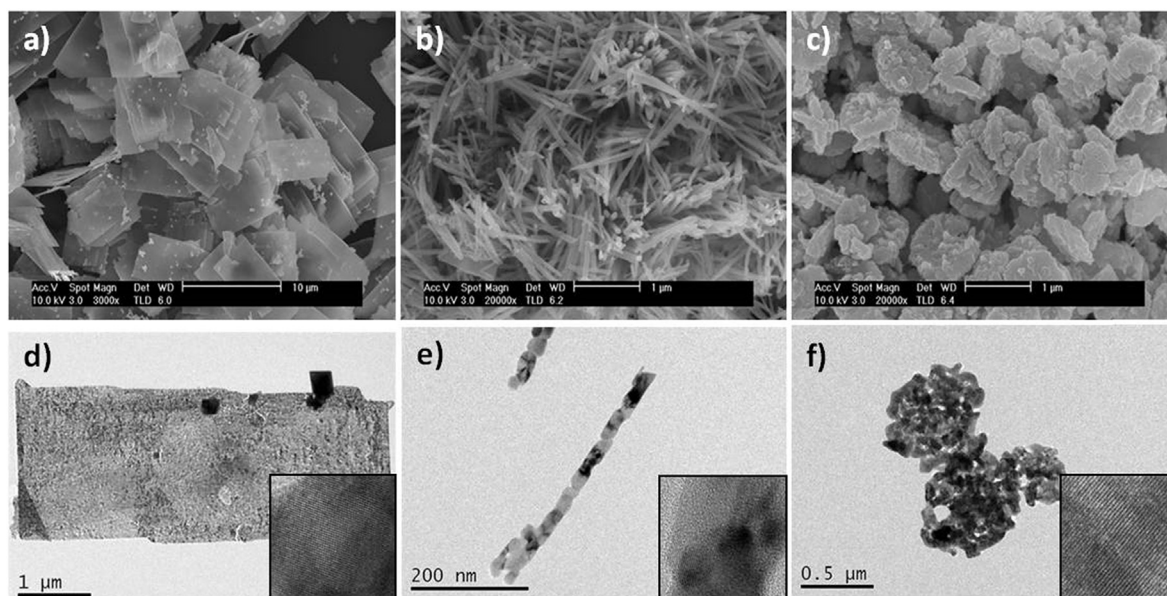
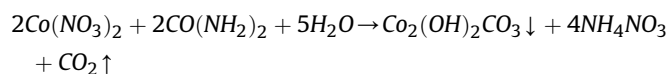


**Fig. 2.** SEM and TEM micrographs of  $\text{CO}_5$  (a, d),  $\text{CO}_N$  (b, e) and  $\text{CO}_F$  (c, f); insets of figures d), e) and f) show magnifications of  $\text{Co}_3\text{O}_4$  crystallites in which lattice fringes are visible.

For hydrothermal synthesis in which urea has been employed as mineralizing agent ( $\text{CO}_5$  and  $\text{CO}_N$ ), the following mechanism was proposed [29]:



The  $\text{Co}_2(\text{OH})_2\text{CO}_3$  primary crystallites formation and agglomeration occur inside the autoclave under vigorous  $\text{CO}_2$  degassing, with a consequent increment in the internal pressure of the system. In condition of low temperature treatment ( $100^\circ\text{C}$  for  $\text{CO}_N$ ), the further agglomeration of crystallites is prevented and the low dimensionality of final species is thus promoted. At higher temperature ( $160^\circ\text{C}$  for  $\text{CO}_5$ ), platelets like structures are instead obtained [26]. Added to this, pH conditions forthcoming the neutrality do not favour any particular crystalline shape formation or, in other words, growth of any particular crystalline facet is promoted [24].

capacity extracted during the first discharge (sodiation),  $\text{CO}_N$  sets the highest value among the materials tested ( $1068 \text{ mAh g}^{-1}$ ), while  $\text{CO}_5$  and  $\text{CO}_F$  lead to considerably lower values ( $770$  and  $789 \text{ mAh g}^{-1}$  respectively). The coulombic efficiencies for the different materials for the first cycle are 70.3%, 70.2% and 71.1% for  $\text{CO}_N$ ,  $\text{CO}_5$  and  $\text{CO}_F$  respectively. By looking at the 1st charge profile (downward black curve in Fig. 4b), three different processes can be recognized: a first small faint step can be located at  $0.8 \text{ V}$  vs.  $\text{Na}/\text{Na}^+$ , followed by a more significant one at  $0.57 \text{ V}$ . The main capacity is connected to the long flat plateau centred at  $0.12 \text{ V}$ . The highest loss in capacity retention, if 1st and 2nd cycle sodiation steps are compared (Fig. 4c–e), is related to the flat plateau occurring at low potential, for all the three materials. This plateau reduces by 72% during the second sodiation, in the case of  $\text{CO}_N$ , in favour of the enhancement of a higher potential plateau that acquires the shape of a leaning line centred around  $0.6 \text{ V}$  (downward red curve), few millivolt above the  $0.57 \text{ V}$  step that becomes itself hardly

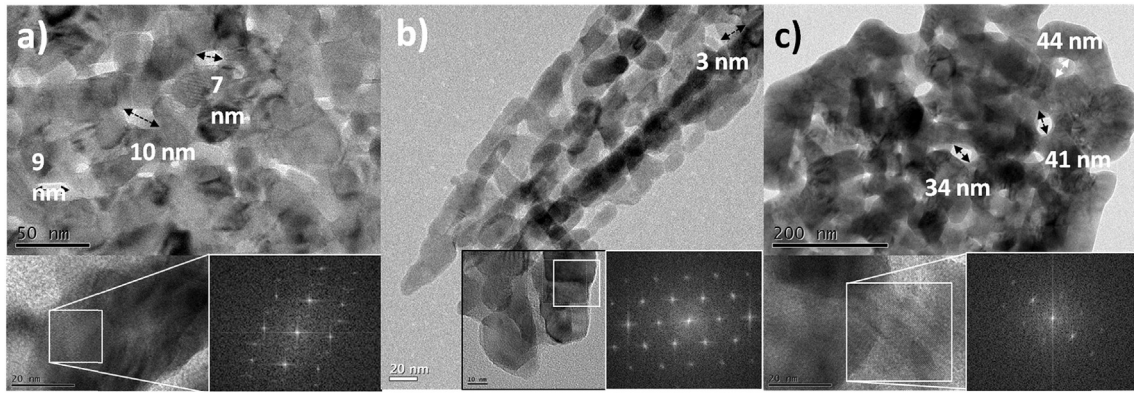


**Fig. 3.** High magnification TEM images of a)  $\text{CO}_5$ , b)  $\text{CO}_N$  and c)  $\text{CO}_F$  samples. Each composition includes a lower magnification image in which some pores are quantified in width; magnifications are different in order to appreciate the fine porous structure of each sample. The inset of each figure shows HRTEM images and the correspondent FFT patterns.

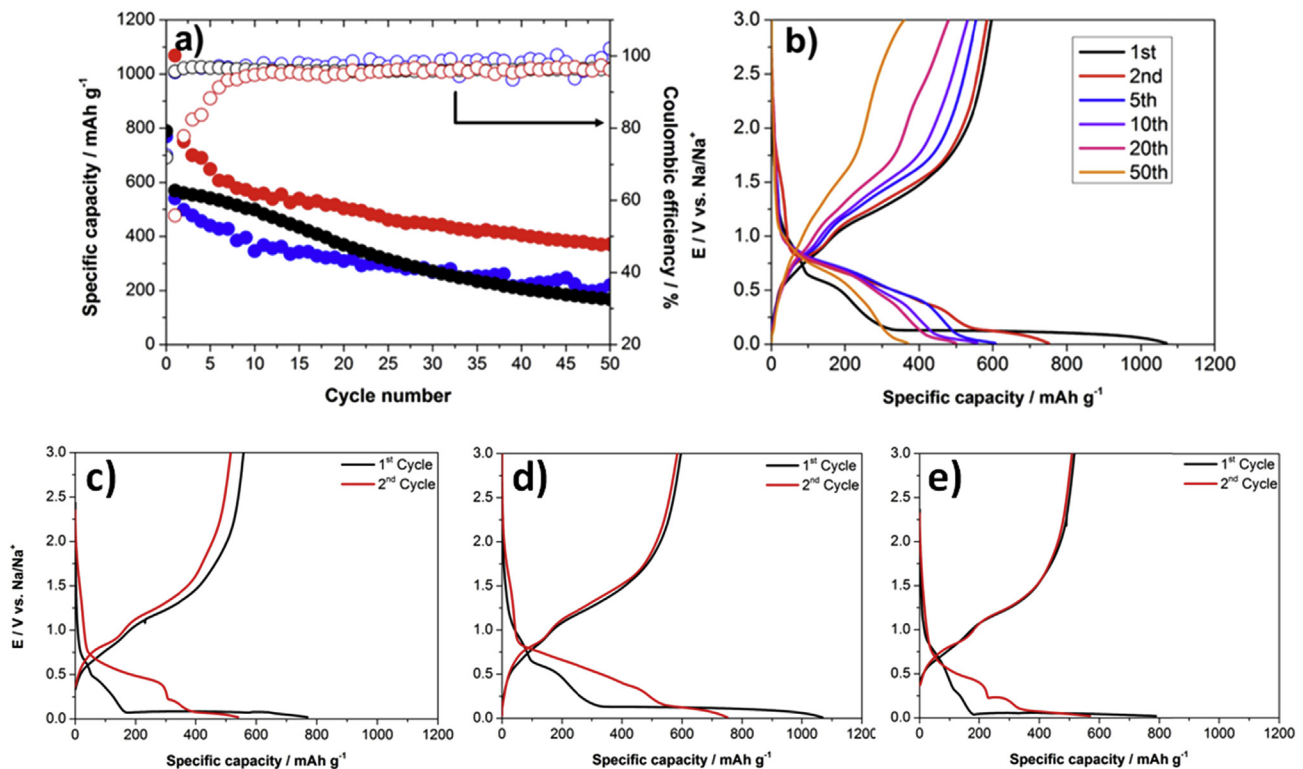


**Fig. 4.** a) Electrochemical characterization of  $\text{Co}_3\text{O}_4$  powders using galvanostatic cycling with potential limitation (GCPL); colors refer to  $\text{CO}_5$  (blue),  $\text{CO}_N$  (red) and  $\text{CO}_F$  (black); b) discharge/charge profiles are reported for  $\text{CO}_N$  sample, all the electrodes have been discharged/charged at 0.1 C ( $89 \text{ mA g}^{-1}$ ); sodiation/desodiation curves of the first two cycles for: c)  $\text{CO}_5$ , d)  $\text{CO}_N$  and e)  $\text{CO}_F$  samples (0.1 C). (For interpretation of the references to colour in this figure legend, the reader is referred to the web version of this article.)

recognisable. The case of  $\text{CO}_5$  and  $\text{CO}_F$  are slightly different, being all the steps shifted at lower potentials and the corresponding plateaus flatter. For what concerns the overpotential between the charge and discharge processes, no appreciable differences were spotted among the materials investigated. The low potential irreversible plateau has not been addressed to sodium interaction with carbon matrix for mainly two reasons: firstly, the capacity extracted from the flat step at 0.2 V is not consistent with the relative amount of Carbon Black included in the electrode formulation (17%). Secondly, as Komaba et al. showed, sodium interaction in hard carbon type conductive matrixes happens close to 0 V and in a wide range of potential values from 3.0 down to 0.5 V vs.  $\text{Na}/\text{Na}^+$  with sloping trends, depending on graphitization level and porosity of carbon

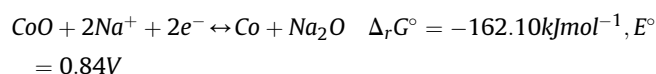
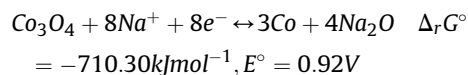
[32]. The possibility of an electrolyte decomposition process forming the SEI layer is also unlikely. It usually occurs over a wider potential window owing the large number of different forming species [21]. The first small plateau at 0.8 V coincides with the formation of the SEI layer [33] while the other processes, including the low potential irreversible step, were attributed to the  $\text{Co}_3\text{O}_4$  reduction to metallic cobalt (Co) [33–35].

The latter process happens in two steps (see discussion hereafter) explaining the two different peaks spotted in the first sodiation [25]. In the following cycles, as demonstrated by *ex-situ* HRTEM analysis conducted by others [34], metallic Co can't be clearly identified as the product of sodiation of the electrode, while  $\text{Na}_2\text{O}$  crystals distinctly appear. In order to shed light onto the

process occurring during the very first cycles, *ex-situ* XRD measurements have been performed as well. In Fig. 5 are reported the diffractograms taken on pristine and cycled electrodes. While in the pristine electrode  $\text{Co}_3\text{O}_4$  diffraction peaks can be easily indexed, the same peaks are not recovered after a full sodiation/de-sodiation cycle; peaks other than those addressable to spinel  $\text{Co}_3\text{O}_4$  appear instead.

Those signals have been attributed to CoO (ICDD card No. 00-078-0431), this would be in contrast with results reported by others that tend to support the complete restoration of  $\text{Co}_3\text{O}_4$  after the first discharge/charge cycle [33]. The formation of a species other than spinel  $\text{Co}_3\text{O}_4$  might be also explicative of the considerable difference between the first and second sodiation profile while the desodiation profile fashion is preserved. Even if not visible in the XRD diffractogram of the cycled electrode, sodium has been detected using energy dispersive X-ray (EDX) analysis (Figs. S1–S3 in Supplementary Material) since from the first cycle. Its presence well supports the thesis on the conversion to CoO phase instead of fully oxidised  $\text{Co}_3\text{O}_4$  and agrees with works present in literature [33,35,36]. The needle-like structures are hardly maintained after sodiation/desodiation cycles and encounter a complete pulverization during the following cycles, as can be clearly spotted by the *ex-situ* SEM micrograph reported in Fig. 6. This process is common to many conversion-like processes, thus it can be inferred that the low dimensionality of the original needle-structures, as distinguishable in Fig. 6a, could drive the easy pulverization of the active materials towards a less dense-packed and somewhat more porous bulk materials (Fig. 6b and c).

After these considerations, two different conversion reactions can be then proposed, taking in account formation of CoO during the first irreversible reduction and the following reversible reaction involving CoO:



An analogous mechanism has been recently proposed for  $\text{Co}_3\text{O}_4$

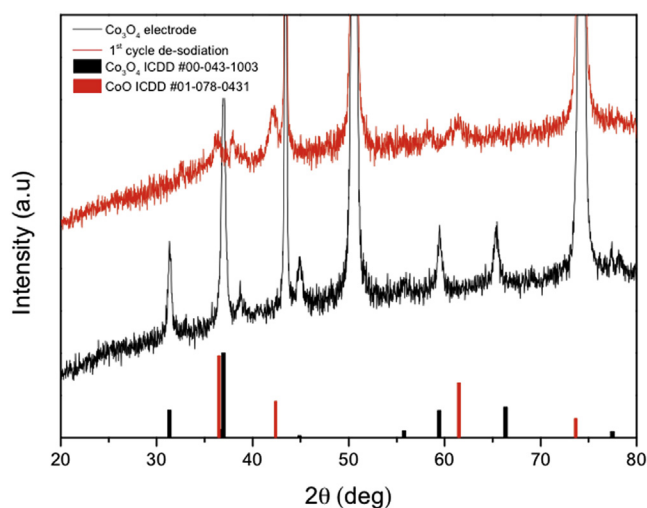


Fig. 5. XRD diffractograms of pristine  $\text{Co}_N$  electrode (black) and cycled one (red). (For interpretation of the references to colour in this figure legend, the reader is referred to the web version of this article.)

lithiation, and together with the SEI formation, would account for the capacity loss afflicting the first cycle [35]. Theoretically speaking, electrochemical de-sodiation of the electrode, giving CoO as the stable oxidised material, instead of  $\text{Co}_3\text{O}_4$ , would be accountable for a reduction in the reversible capacity from  $890 \text{ mAh g}^{-1}$ , to  $668 \text{ mAh g}^{-1}$  (–25%). Considering the total capacity loss related to the first cycle, the residual capacity loss, not ascribable to CoO conversion mechanism, would be comprised between 3.8% and 4.7% of the initial capacity, depending on the  $\text{Co}_3\text{O}_4$  initial morphology. Indeed the residual capacity loss would be directly correlated to the SEI layer formation whose entity is strongly bonded to the total surface area of the active material.

The rate test of the promising  $\text{Co}_N$  has been performed and results are reported in Fig. 7a. Capacity extracted progressively decrease with the rising in the charge/discharge current as expected. Nevertheless, at 5 C ( $4470 \text{ mA g}^{-1}$ ) a surprisingly high capacity of  $160 \text{ mAh g}^{-1}$  is obtained. When the current is set back to 0.1 C ( $89 \text{ mA g}^{-1}$ ) a reversible capacity of  $415 \text{ mAh g}^{-1}$  can still be achieved. The value at 5 C sets, as far as we know from the literature, a new mile stone in the high rate performance for nanostructured cobalt oxide devoid of a conductive substrate, employed in sodium ion batteries. In recent works, discrete capacities have been obtained using high current drains (with  $3200 \text{ mA g}^{-1}$  as maximum [31]) from composite materials in which a conductive matrix, namely carbon nanotubes or reduced graphene oxide sheets, took upon itself an effective electron conductivity inside the bulk of the material. Since in this case no conductive substrate has been employed, a part from the carbon black for electrode formulation, all the spotted favourable features must be addressed to the active material itself. In particular, high rate capabilities can be related to i) the thickness of the needles and the nanometric sized particles that offer a short path to sodium diffusion and electron motion, and ii) higher degree of freedom of nanometric particles arranged in a 1D fashion in bearing the volume variations during sodiation and de-sodiation processes. As comparison, in the recent work by Ahmad et al. [25],  $83 \text{ mAh g}^{-1}$  were obtained at  $500 \text{ mA g}^{-1}$  using cobalt oxide nanoplatelets grafted onto reduced graphene oxide sheets.

The increase in scan rates does not appeared to change sensibly the charge/discharge profiles appearance, as can be clearly seen in Fig. 7b. Nonetheless, stepping from 5 C back to 0.1 C determines the appearance of a slight hump in the desodiation curve around 2.0 V, whose origin is not clear. As observed in multiple other oxide-based materials, the hysteresis between charge and discharge curves increases slightly as the charge/discharge current goes up. As previously quoted in the present work, the irreversible capacity affecting the first cycle is a major concern for a possible application of the technology. The irreversible process accountable for the capacity loss, being either SEI formation or an irreversible conversion reaction step as hypothesized by Du et al. [35], represents a massive sodium consumption inside the cell, and it's not an acceptable compromise assumed the high theoretical capacity of the active material. This observation led, as a possible solution, to a chemical pre-sodiation of the electrode in order to pre-condition the active material supplying the sodium that would otherwise come from the cathode once assembled the cell. Similar treatments have been used in preparing materials for other types of anodes [37,38], but employing it with a conversion compound might be surpassingly useful in order to direct the conversion reaction to a well-defined and thermodynamically driven product. The sodium uptake has been assessed with an elemental analysis (AAS) in order to highlight the dependence with the sodiation times (Table 2).

Since the sodium amount detected was the same for the 60 and 90 min sodiation, respectively, the first condition was considered the required amount of time to obtain the saturation of the

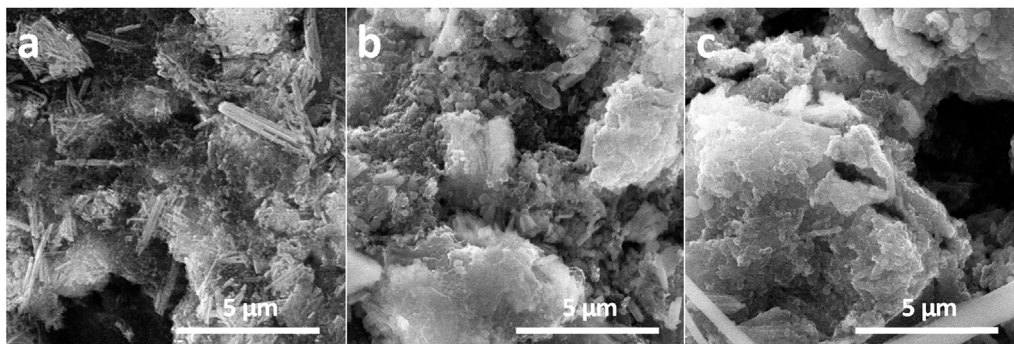


**Fig. 6.** SEM micrographs of  $\text{CO}_N$  electrode at different times during GCPLT tests; a) the pristine electrode, the electrodes after b) 1 cycle, and c) 4 cycles. The coin cells after GCPL tests were disassembled and washed with anhydrous acetonitrile to remove Na salts and SEI layers inside the Ar-filled glove box.

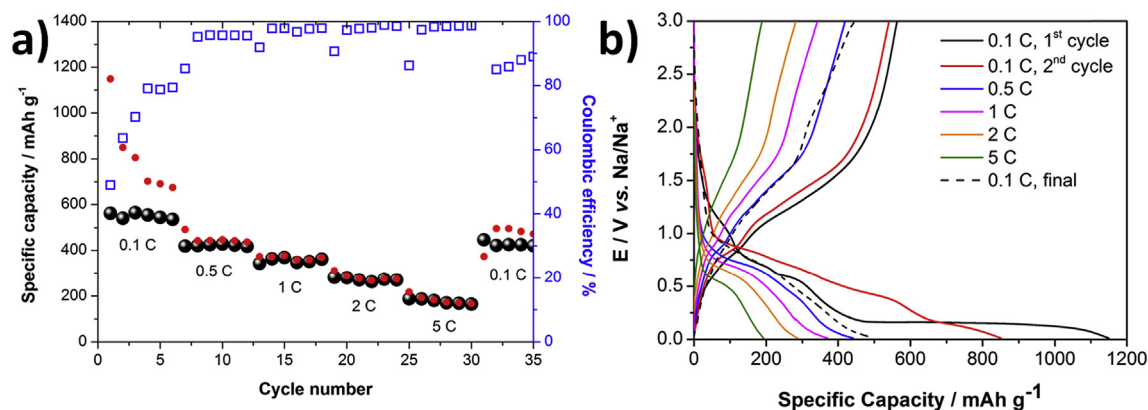


**Fig. 7.** a) Rate capability tests on  $\text{CO}_N$  at different C-rates of 0.1C ( $89 \text{ mA g}^{-1}$ ), 0.5C ( $445 \text{ mA g}^{-1}$ ), 1C ( $890 \text{ mA g}^{-1}$ ), 2C ( $1780 \text{ mA g}^{-1}$ ), 5C ( $4450 \text{ mA g}^{-1}$ ). For each current density, six cycles have been performed. b) Charge/discharge profiles obtained from the rate tests performed on  $\text{CO}_N$  sample. The last cycle performed at low rate (0.1 C) is displayed with the black-dashed line.

electrode. In Fig. 8a, 1st and 2nd cycle profiles of pre-sodiated and pristine  $\text{CO}_N$  electrode are reported. The severe reduction in the irreversible capacity is clearly visible, furthermore a sensibly different charge/discharge profile is also achieved. The long lasting plateau at 0.12 V is indeed completely suppressed in favour of a shorter process occurring at higher potential (0.31 V) that has its correspondent recognisable event above 1 V, in the upward discharge curve. Owing the similarities between charge/discharge

**Table 2**

Sodium uptake evaluated using AAS correlated to sodiation times.

Sodiation time/min	x in $\text{Na}_x\text{CO}_3\text{O}_4$
30	0.94
60	1.50
90	1.50

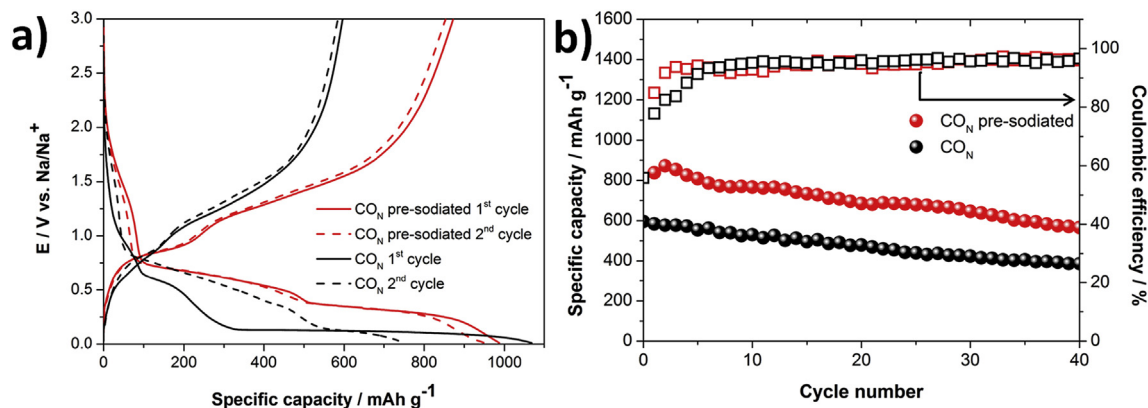


**Fig. 8.** a) Sodiation/desodiation profiles of pre-treated (red) and pristine (black)  $\text{CO}_N$  electrode, solid and dashed lines refer to first and second cycle respectively; b) cycling stability and Coulombic efficiency of the two electrodes, namely  $\text{CO}_N$  pristine (black) and  $\text{CO}_N$  pre-sodiated (red). Tests taken at 0.1 C ( $89 \text{ mA g}^{-1}$ ). (For interpretation of the references to colour in this figure legend, the reader is referred to the web version of this article.)

profile of pre-sodiated electrodes and second cycle profile of electrochemically sodiated/desodiated ones, a parallelism between the mechanism highlighted via *ex-situ* XRD characterization and the chemical sodiation products can be sketched. CoO, rather than Co<sub>3</sub>O<sub>4</sub>, can be recognized as the electrochemically stable species in a chemically reducing environment, and might be also addressed as the most oxidised state of cobalt recovered after the desodiation of chemically treated electrodes. The thermodynamic of chemical sodiation of cobalt oxide is associated with a highly spontaneous process characterized by the  $\Delta_r G^\circ$  value of  $-710.30 \text{ kJ mol}^{-1}$ . This has a direct correlation with the considerable lattice energy ( $\Delta_{\text{lattice}} H^\circ$ ) of the corresponding product of the conversion reaction (Na<sub>2</sub>O):  $1239 \text{ kJ mol}^{-1}$ , the highest among sodium chalcogenides, halides and hydrides [11]. Owing these considerations, the conversion reaction expected during the electrodes pre-treatment is the complete conversion of Co<sub>3</sub>O<sub>4</sub> to metallic cobalt. We can thus conclude that the pre-conditioning of electrodes positively direct following sodiation/desodiation processes by ensuring a complete reduction of Co<sub>3</sub>O<sub>4</sub> to metal Co. Persistency of Co<sub>3</sub>O<sub>4</sub> in the electrode through cycling has to be then considered as a deleterious agent for a correct and stable operation, and a chemical sodiation of the electrode provides a complete and effective conversion of the totality of Co<sub>3</sub>O<sub>4</sub> to metal Co. The electrochemical sodiation, on the contrary, still represents a controversial and somewhat inefficient approach that involves a heterogeneous process (partial reduction of Co<sub>3</sub>O<sub>4</sub> to metal Co, SEI formation and other decomposition products) far to be extensively understood.

Nevertheless standard electrochemical studies on different morphologies of the Co<sub>3</sub>O<sub>4</sub> precursor, have stressed the importance of high aspect ratio and low dimensionality primary particles agglomerates in indexing a more efficient conversion reaction and in sensibly affecting the overall performances of the sodium half cell.

The beneficial effect of the pre-sodiation can be spotted also throughout all the cycles in Fig. 8b. Interestingly, the low starting OCV of the pre-treated electrode ( $\sim 0.4 \text{ V vs Na/Na}^+$ ) suggests a heavily sodiated state of the active material, for this reason the galvanostatic cyclation started with a charging step (de-sodiation). Differently, CO<sub>F</sub> could not be chemically completely sodiated. After coin cell assembling, an open circuit potential of 1.5 V is measured, denoting only a partial sodium uptake. Thus a further positive current step has been employed in this case in order to reach the complete sodiation of the electrode (Fig. S5 in Supplementary Material). A general higher specific capacity is obtained, presumably thanks to the smaller amount of active material compromised during the electrochemical sodiation involved in the first cycle. Starting capacity value for the sodiated electrode,  $987 \text{ mAh g}^{-1}$ , is above the theoretical value previously discussed ( $668 \text{ mAh g}^{-1}$ ) and this might be due to SEI layer formation as well as to parasitic processes occurring during first cycles. However, the large irreversible capacity above the theoretical value is sensibly reduced. Another aspect worth to be noted is that the inevitable capacity fading through cycling does not follow an exponential decay in the very first cycles, as occurs for a common Co<sub>3</sub>O<sub>4</sub> electrode. The capacity loss sticks more to a linear decay starting from a capacity value, considering the irreversible processes taking place in the first cycles, only  $100 \text{ mAh g}^{-1}$  above the theoretical value. After 50 cycle, the reversible capacity,  $508 \text{ mAh g}^{-1}$ , still lies above the value of the pristine Co<sub>3</sub>O<sub>4</sub> electrode,  $348 \text{ mAh g}^{-1}$ . As can be observed from Figs. S4 and S5 in Supplementary Material, CO<sub>S</sub> and CO<sub>F</sub> subjected to the same pre-sodiation treatment did not show the same behavior as CO<sub>N</sub>. Despite CO<sub>S</sub> showed a higher immediate capacity and a reduction of the initial irreversible process, its capacity was degraded rapidly after 50 cycles, matching with cycling behavior of the pristine electrode. Furthermore, the pre-sodiated CO<sub>F</sub> electrode delivers lower capacities and worse cycling capability compared to

pristine one. These results prove that CO<sub>N</sub> needle-like structure carries out also a positive influence during the chemical sodiation, while more three-dimensional structures (slabs and flakes) are clearly not suitable for a chemical sodiation pre-treatment.

#### 4. Conclusions

In the present work, a cost effective and easy to reproduce synthetic path has been proposed to easily modulate the morphological characteristics of a spinel-Co<sub>3</sub>O<sub>4</sub> hierarchical structure. The modulation of the synthetic parameters allowed to obtain primary nanometric sized crystalline particles aggregation in different hierarchical structures. During the preparation route, no conductive substrate was employed in order to effectively isolate the behavior of Co<sub>3</sub>O<sub>4</sub> morphologies alone. Three morphologies have been extensively characterized under the electrochemical point of view. For the first time, at the best of our knowledge, a needle like structure was obtained for Co<sub>3</sub>O<sub>4</sub> employed as an anode material in sodium ion batteries. A high porosity and high aspect ratio of agglomerates seem to facilitate the electrochemical processes involving the active material. The most promising among the structure investigated, CO<sub>N</sub>, assured discrete performances in galvanostatic tests and considerable reversible capacities were also obtained high operational currents up to 5 C. Finally, the beneficial effect of a pre-sodiation treatment directly on the electrodes was also highlighted, and should be kept as a viable alternative to the electrochemical performance optimization of conversion materials for sodium ion batteries. This research aims to encourage further studies around conversion materials for sodium ion batteries, since they might really play a relevant role in the design of future low cost battery technologies. The presented results and experiments still display room for additional improvement (capacity stability, general reliability of the material and irreversible capacity reduction), but positively tackle some of the challenges on conversion anode materials for SIBs still hold nowadays.

#### Acknowledgments

Italian authors are gratefully to the Ministero degli Affari Esteri e della Cooperazione Internazionale to support the bilateral Italian/Korean project of international cooperation (contract KR16GR05) and Korean authors thanks to National Research Foundation (NRF) of Korea (NRF-2016K1A3A1A25003532). This work was also supported by the Program to Solve Climate Changes (NRF-2010-1AAA001-2010-0029031) of Korea (NRF) funded by the Ministry of Science, ICT and Future Planning and by the Climate Change Research Hub of KAIST (Grant No. N1160019).

#### Appendix A. Supplementary data

Supplementary data related to this article can be found at <http://dx.doi.org/10.1016/j.jpowsour.2016.09.094>.

#### References

- [1] J.B. Goodenough, K. Park, The Li-Ion rechargeable Battery: a perspective, *J. Am. Chem. Soc.* 135 (4) (2013) 1167–1176, <http://dx.doi.org/10.1021/ja3091438>.
- [2] J.M. Tarascon, M. Armand, Issues and challenges facing rechargeable lithium batteries, *Nature* 414 (2001) 359–367, <http://dx.doi.org/10.1038/35104644>.
- [3] M. Armand, J.-M. Tarascon, Building better batteries, *Nature* 451 (2008) 652–657, <http://dx.doi.org/10.1038/451652a>.
- [4] J.-M. Tarascon, Is lithium the new gold? *Nat. Chem.* 2 (2010) 510, <http://dx.doi.org/10.1038/nchem.680>.
- [5] M. Dahbi, N. Yabuuchi, K. Kubota, K. Tokiwa, S. Komaba, Negative electrodes for Na-ion batteries, *Phys. Chem. Chem. Phys.* (2014), <http://dx.doi.org/10.1039/c4cp00826j>.
- [6] Y. Kim, K.-H. Ha, S.M. Oh, K.T. Lee, High-capacity anode materials for sodium-ion batteries, *Chemistry* 20 (2014) 11980–11992, <http://dx.doi.org/10.1002>

- chem.201402511.
- [7] M.D. Slater, D. Kim, E. Lee, C.S. Johnson, Sodium-ion batteries, *Adv. Funct. Mater.* 23 (2013) 947–958, <http://dx.doi.org/10.1002/adfm.201200691>.
- [8] V. Chevrier, G. Ceder, Challenges for Na-ion negative electrodes, *J. Electrochem. Soc.* 158 (2011) A1011, <http://dx.doi.org/10.1149/1.3607983>.
- [9] Y.H. Ung, C.H. Lim, D.K. Kim, Graphene-supported Na<sub>3</sub>V<sub>2</sub>(PO<sub>4</sub>)<sub>3</sub> as a high rate cathode material for sodium-ion batteries, *J. Mater. Chem. A* 1 (2013) 11350, <http://dx.doi.org/10.1039/c3ta12116j>.
- [10] C. Masquelier, L. Croguennec, Polyanionic (phosphates, silicates, sulfates) frameworks as electrode materials for rechargeable Li (or Na) batteries, *Chem. Rev.* 113 (2013) 6552–6591, <http://dx.doi.org/10.1021/cr3001862>.
- [11] F. Klein, B. Jache, A. Bhide, P. Adelhelm, Conversion reactions for sodium-ion batteries, *Phys. Chem. Chem. Phys.* 15 (2013) 15876–15887, <http://dx.doi.org/10.1039/c3cp52125g>.
- [12] X. Xia, J.R. Dahn, Study of the reactivity of Na/Hard carbon with different solvents and electrolytes, *J. Electrochem. Soc.* 159 (2012) A515, <http://dx.doi.org/10.1149/2jes111637>.
- [13] R.J. White, K. Tauer, M. Antonietti, M.M. Titirici, Functional hollow carbon nanospheres by latex templating, *J. Am. Chem. Soc.* 132 (2010) 17360–17363, <http://dx.doi.org/10.1021/ja107697s>.
- [14] T. Chen, Y. Liu, L. Pan, T. Lu, Y. Yao, Z. Sun, et al., Electrospun carbon nanofibers as anode materials for sodium ion batteries with excellent cycle performance, *J. Mater. Chem. A* 2 (2014) 4117, <http://dx.doi.org/10.1039/c3ta14806h>.
- [15] J. Qian, Y. Chen, L. Wu, Y. Cao, X. Ai, H. Yang, High capacity Na-storage and superior cyclability of nanocomposite Sb/C anode for Na-ion batteries, *Chem. Commun. (Camb.)* 48 (2012) 7070–7072, <http://dx.doi.org/10.1039/c2cc32730a>.
- [16] M. He, K.V. Kravchik, M. Walter, M.V. Kovalenko, Monodisperse antimony nanocrystals for high-rate Li-ion and Na-ion battery anodes: nano versus bulk, *Nano Lett.* 14 (2014) 1255–1262, <http://dx.doi.org/10.1021/nl404165c>.
- [17] Y. Wang, D. Su, C. Wang, G. Wang, SnO<sub>2</sub>@MWCNT nanocomposite as a high capacity anode material for sodium-ion batteries, *Electrochem. Commun.* 29 (2013) 8–11, <http://dx.doi.org/10.1016/j.elecom.2013.01.001>.
- [18] B. Farbod, K. Cui, W.P. Kalisvaart, M. Kupsta, B. Zahiri, A. Kohandehghan, et al., Anodes for sodium ion batteries based on tin-germanium-antimony alloys, *ACS Nano* 8 (2014) 4415–4429, <http://dx.doi.org/10.1021/nn4063598>.
- [19] L. Xiao, Y. Cao, J. Xiao, W. Wang, L. Kovarik, Z. Nie, et al., High capacity, reversible alloying reactions in SnSb/C nanocomposites for Na-ion battery applications, *Chem. Commun. (Camb.)* 48 (2012) 3321–3323, <http://dx.doi.org/10.1039/c2cc17129e>.
- [20] P.R. Kumar, Y.H. Jung, K.K. Bharathi, C.H. Lim, D.K. Kim, High capacity and low cost spinel Fe<sub>3</sub>O<sub>4</sub> for the Na-ion battery negative electrode materials, *Electrochim. Acta* 146 (2014) 503–510, <http://dx.doi.org/10.1016/j.electacta.2014.09.081>.
- [21] D. Su, X. Xie, P. Munroe, S. Dou, G. Wang, Mesoporous hexagonal Co<sub>3</sub>O<sub>4</sub> for high performance lithium ion batteries, *Sci. Rep.* 4 (2014) 6519, <http://dx.doi.org/10.1038/srep06519>.
- [22] S. Yuan, X.L. Huang, D.L. Ma, H.G. Wang, F.Z. Meng, X.B. Zhang, Engraving copper foil to give large-scale binder-free porous CuO arrays for a high-performance sodium-ion battery anode, *Adv. Mater.* 26 (2014) 2273–2279, <http://dx.doi.org/10.1002/adma.201304469>.
- [23] J. Guo, L. Chen, X. Zhang, H. Chen, Porous Co<sub>3</sub>O<sub>4</sub> nanorods as anode for lithium-ion battery with excellent electrochemical performance, *J. Solid State Chem.* 213 (2014) 193–197, <http://dx.doi.org/10.1016/j.jssc.2014.02.036>.
- [24] X. Xiao, X. Liu, H. Zhao, D. Chen, F. Liu, J. Xiang, et al., Facile shape control of Co<sub>3</sub>(O<sub>4</sub>) and the effect of the crystal plane on electrochemical performance, *Adv. Mater.* 24 (2012) 5762–5766, <http://dx.doi.org/10.1002/adma.201202271>.
- [25] Y. Liu, Z. Cheng, H. Sun, H. Arandiyani, J. Li, M. Ahmad, Mesoporous Co<sub>3</sub>O<sub>4</sub> sheets/3D graphene networks nanohybrids for high-performance sodium-ion battery anode, *J. Power Sources* 273 (2015) 878–884, <http://dx.doi.org/10.1016/j.jpowsour.2014.09.121>.
- [26] J.S. Chen, T. Zhu, Q.H. Hu, J. Gao, F. Su, S.Z. Qiao, et al., Shape-controlled synthesis of cobalt-based nanocubes, nanodiscs, and nanoflowers and their comparative lithium-storage properties, *ACS Appl. Mater. Interfaces* 2 (2010) 3628–3635, <http://dx.doi.org/10.1021/am100787w>.
- [27] J. Ming, H. Ming, W.-J. Kwak, C. Shin, J. Zheng, Y.-K. Sun, The binder effect on an oxide-based anode in lithium and sodium-ion battery applications: the fastest way to ultrahigh performance, *Chem. Commun. (Camb.)* 50 (2014) 13307–13310, <http://dx.doi.org/10.1039/c4cc02657h>.
- [28] M.M. Rao, B.R. Reddy, M. Jayalakshmi, V.S. Jaya, B. Sridhar, Hydrothermal synthesis of Mg-Al hydrotalcites by urea hydrolysis, *Mater. Res. Bull.* 40 (2005) 347–359, <http://dx.doi.org/10.1016/j.materresbull.2004.10.007>.
- [29] L. Cui, J. Li, X.G. Zhang, Preparation and properties of Co<sub>3</sub>O<sub>4</sub> nanorods as supercapacitor material, *J. Appl. Electrochem.* (2009), <http://dx.doi.org/10.1007/s10800-009-9891-5>.
- [30] Q. Deng, L. Wang, J. Li, Electrochemical characterization of Co<sub>3</sub>O<sub>4</sub>/MCNTs composite anode materials for sodium-ion batteries, *J. Mater. Sci.* 50 (2015) 4142–4148, <http://dx.doi.org/10.1007/s10853-015-8975-3>.
- [31] Z. Jian, P. Liu, F. Li, M. Chen, H. Zhou, Monodispersed hierarchical Co<sub>3</sub>O<sub>4</sub> spheres intertwined with carbon nanotubes for use as anode materials in sodium-ion batteries, *J. Mater. Chem. A* 2 (2014) 13805, <http://dx.doi.org/10.1039/C4TA02516D>.
- [32] S. Komaba, W. Murata, T. Ishikawa, N. Yabuuchi, T. Ozeki, T. Nakayama, et al., Electrochemical Na insertion and solid electrolyte interphase for hard-carbon electrodes and application to Na-ion batteries, *Adv. Funct. Mater.* 21 (2011) 3859–3867, <http://dx.doi.org/10.1002/adfm.201100854>.
- [33] M.M. Rahman, A.M. Glushenkov, T. Ramireddy, Y. Chen, Electrochemical investigation of sodium reactivity with nanostructured Co<sub>3</sub>O<sub>4</sub> for sodium-ion batteries, *Chem. Commun. (Camb.)* 50 (2014) 5057–5060, <http://dx.doi.org/10.1039/c4cc01033g>.
- [34] M. Rahman, I. Sultana, Z. Chen, M. Srikanth, L.H. Li, X.J. Dai, et al., Ex situ electrochemical sodiation/desodiation observation of Co<sub>3</sub>O<sub>4</sub> anchored carbon nanotubes: a high performance sodium-ion battery anode produced by pulsed plasma in a liquid, *Nanoscale* (2015) 13088–13095, <http://dx.doi.org/10.1039/c5nr03335g>.
- [35] Q. Su, J. Zhang, Y. Wu, G. Du, Revealing the electrochemical conversion mechanism of porous Co<sub>3</sub>O<sub>4</sub> nanoplates in lithium ion battery by in situ transmission electron microscopy, *Nano Energy* 9 (2014) 264–272, <http://dx.doi.org/10.1016/j.nanoen.2014.08.006>.
- [36] J. Yang, T. Zhou, R. Zhu, X. Chen, Z. Guo, J. Fan, et al., Highly ordered dual porosity mesoporous cobalt oxide for sodium-ion batteries, *Adv. Mater. Interfaces* 3 (2016) 1–7, <http://dx.doi.org/10.1002/admi.201500464>.
- [37] J. Hassoun, F. Bonaccorso, M. Agostini, M. Angelucci, M.G. Betti, R. Cingolani, et al., An advanced lithium-ion battery based on a graphene anode and a lithium iron phosphate cathode, *Nano Lett.* 14 (2014) 1–17, <http://dx.doi.org/10.1021/nl502429m>.
- [38] E. De La Llave, V. Borgel, K.J. Park, J.Y. Hwang, Y.K. Sun, P. Hartmann, et al., Comparison between Na-ion and Li-ion cells: understanding the critical role of the cathodes stability and the anodes pretreatment on the cells behavior, *ACS Appl. Mater. Interfaces* 8 (2016) 1867–1875, <http://dx.doi.org/10.1021/acsami.5b09835>.